Article

Hybrid Guidance Optimization for Multipulse Glideslope Approach with Bearing-Only Navigation

Hao Yuan * , **Dongxu Li and Jie Wang**

College of Aerospace Science and Engineering, National University of Defense Technology,
Changsha 410073, China; dongxuli@nudt.edu.cn (D.L.); wangjie@nudt.edu.cn (J.W.)
* Correspondence: yuanhao11@nudt.edu.cn

Abstract: This paper proposes a modified glideslope guidance method that optimizes a hybrid multiobjective of bearing-only navigation error and fuel consumption. The traditional glideslope guidance fixes uniform maneuver intervals and the initial approach velocity as a predetermined value, making this approach inflexible. In this paper, the maneuver intervals and the initial approach velocity were used as optimization variables, and a hybrid cost function was designed. The tradeoff between the two objectives was analyzed with a bearing-only navigation simulation conducted to reveal the navigation performance following different resulting trajectories. The result showed that the optimal scheduled times of maneuvers remained relatively stable under different tradeoff weights, while a strong correlation between the optimal initial approach velocity and the tradeoff weight was revealed. Therefore, when the optimization has to be solved several times online with different tradeoff weights, the initial approach velocity can be the only optimization variable, leaving the scheduled times of maneuvers fixed in the optimal values achieved offline. These findings provide a potential reference for far-approach trajectory design of bearing-only navigation.

Keywords: guidance optimization; multipulse glideslope; far approach to small celestial bodies; bearing-only navigation

1. Introduction

Small celestial body missions are popular with different mission profiles, such as impactors [1], high-speed flybys [2], orbiters [3], landers [4], and sample returns [5–7], because they cannot only promote space technology to defend the Earth, but also help us understand the origin and evolution of the solar system [8].

The far-approach phase is necessary for all small celestial body missions [9,10]. It is the key phase where the interplanetary transfer ends and the detection of the asteroid begins [11]. Due to the orbit propagation error and the maneuver execution error during the interplanetary transfer phase, as well as the error of the asteroid ephemeris, far-approach guidance is necessary to arrive at a relative range and accuracy that will allow the start of close-approach autonomous operations.

The far-approach guidance of the spacecraft usually realizes the optimization of some performance indices (such as fuel consumption or rendezvous time) under multiple constraints. This generally requires that the original problem to be constructed as an optimal control problem (OCP), such as linear programming (LP), quadratic programming (QP), quadratically constrained quadratic programming (QCQP), second-order cone programming (SOCP), and mixed integer programming (MIP) [12–14]. These problems are generally solved by the active set or interior point method [3]. Due to the high sensitivity of open-loop rendezvous guidance in the face of uncertain conditions, autonomous guidance generally requires such an optimal control problem to be embedded into the closed-loop feedback system, in which the real-time estimation of the state by the navigation system is used as the input of the closed-loop guidance. In the closed-loop feedback guidance architecture,

the optimal control problem needs to be solved repeatedly with a receding time horizon and using current navigation filter estimates to set the initial conditions (ICs) for the optimization, which corresponds to model predictive control in spacecraft rendezvous [15]. This puts forward high requirements for computational efficiency when repeatedly solving the optimal control problem. In addition, Hablani proposed a multipulse glideslope guidance method based on the Clohessy–Wiltshire (CW) equation [16], which was used for rendezvous and proximity operations of the Space Shuttle because of its advantages of an arbitrary design of the approximation direction, gradual reduction of the relative distance and relative speed, prevention of collision, and safety. However, these guidance methods usually fix uniform maneuver intervals and do not consider the optimization of the scheduled times of maneuvers. Benedikter discretizes the independent variable over a dense time grid to optimize the scheduled times of maneuvers, which is a viable choice, despite one that makes the problem more complex [17].

In recent years, some researchers have taken navigation performance into consideration in guidance method design [18]. During the far-approach phase to a small celestial body, the spacecraft is far from the body, and the available relative measurement sensor is generally only a narrow field camera. Therefore, the uniqueness of the asteroid far-approach guidance design lies in the fact that the limited available sensors necessitate the observability and navigation accuracy of relative angle-only navigation (AON) [19]. Based on the geometric interpretation of maneuvers in angle-only rendezvous, Woffinden and Geller proposed observability criteria for AON and developed an analytical solution of the maneuver for optimizing observability [19,20]. Subsequently, Grzymisch et al. derived a simpler closed form of the observability criteria from the concept of linear uncorrelation, analytically obtained optimal observability maneuvers and proposed an optimal rendezvous guidance method with enhanced angle-only observability [18,21,22]. Mok et al. defined an observability measurement derived from the Fisher information matrix (FIM) and the Cramér–Rao lower bound (CRLB) and added this measurement to the optimization objective function to obtain a multipulse rendezvous guidance law [23]. Based on an angle-only measurement equation with pseudorange measurement, Hou et al. used the FIM and the CRLB to estimate navigation accuracy, providing another observability criterion. The sum of the CRLB at each observation time during the whole process was taken as the objective function of single maneuver rendezvous optimization [24]. In addition to theoretical research, an angle-only rendezvous on-orbit test was conducted at the end of the PRISMA mission [25]. In this test, the orbit maneuver of the spacecraft was planned offline to maintain the desired formation configuration, and observability was used to select a better strategy from the solved rendezvous strategy set. Generally, the above studies also fix uniform maneuver intervals. They are suitable for missions with short rendezvous times [26].

In our work, navigation accuracy optimization, fuel consumption optimization, and multipulse glideslope guidance are combined to realize a multipulse glideslope guidance method with an enhanced navigation accuracy. The scheduled times of maneuvers and the initial approach velocity are used as optimization variables to reveal their influence on the far approach guidance. The proposed method retains the advantages of the multipulse glideslope guidance method, including on-demand approach direction design and the decreasing approach speed with the distance, and adds the optimization of the mixed index of AON accuracy and fuel consumption. It is an attractive choice for the approach trajectory design of a small celestial body mission.

The structure of this paper is organized as follows. First, the navigation accuracy criteria based on the FIM are given in Section 2. Then, Section 3 introduces traditional multipulse glideslope guidance and analyzes its potential independent variables. In Section 4, an offline multipulse glideslope guidance method with a hybrid optimization of the navigation accuracy and fuel consumption is proposed. Then, simulation results are given in Section 5, and the influence of the weight of navigation accuracy vs. fuel consumption is analyzed. Finally, Section 6 concludes with some interesting findings.

2. Navigation Accuracy Criteria Based on the FIM

2.1. AON System with an Orbit Maneuver

For convenience, researchers usually study AON based on the orbital relative motion equations—the CW equations [27]—under the assumption of a circular orbit and short rendezvous times. However, the orbit of small celestial bodies around the Sun is generally nonnegligibly elliptical, and the far approach to small celestial bodies lasts a long time. In this paper, the Tschauner–Hempel (TH) equation [28] under the assumption of an elliptical orbit is adopted, which also has an analytical homogeneous solution [29], similar to the CW equations. After an impulse maneuver $\boldsymbol{u}$, the relative motion equation can be written as follows:

$$\boldsymbol{x}(t) = \boldsymbol{\Phi}(t)\boldsymbol{x}_0 + \mathbf{G}(t)\boldsymbol{u}. \tag{1}$$

The equation is defined in the asteroid Hill rotation coordinate system (see Appendix A and Figure A1), where $\boldsymbol{x}_0$ is the state vector at the initial maneuver time and $\boldsymbol{x}$ is the state vector at time t after the impulse maneuver. See Appendix B for the definitions of state transition matrix $\boldsymbol{\Phi}(t)$ and input matrix $\mathbf{G}(t)$, which are subsequently abbreviated as $\boldsymbol{\Phi}$ and $\mathbf{G}$, respectively, and their block matrix form.

The angle-only measurement equation based on the orbital maneuver includes the real measurement of azimuth angle θ and elevation angle ϕ of the spacecraft relative to the target small celestial body and the pseudo measurement of distance d of the spacecraft relative to the target, as shown in Figure A2 of Appendix C. The measurement equation can be written in the following form:

$$
\begin{aligned}
\boldsymbol{y} = \boldsymbol{h}(\boldsymbol{x}) + \boldsymbol{v} &\equiv \begin{bmatrix} \theta \\ \phi \\ d \end{bmatrix} + \begin{bmatrix} v_\theta \\ v_\phi \\ v_d \end{bmatrix} \\
&= \begin{bmatrix} \arctan(z/y) \\ \arcsin\left(x/\sqrt{x^2 + y^2 + z^2}\right) \\ \sqrt{x^2 + y^2 + z^2} \end{bmatrix} + \begin{bmatrix} v_\theta \\ v_\phi \\ v_d \end{bmatrix}
\end{aligned}
\tag{2}
$$

where x, y, and z are relative position coordinates as defined in Appendix A, v_θ and v_ϕ are angle measurement error noise, the covariance is known as $R_{\theta,\phi}$, and v_d is the pseudorange measurement error noise based on the angle measurement noise.

2.2. Pseudorange Measurement and Its Error Noise

The orbit maneuver provides potential range information for AON, and a pseudorange measurement can be built to describe it. However, pseudorange measurements based on the orbit maneuver bring errors. The relationship between the pseudorange measurement error and the angle measurement error has been analyzed [20,24]. Previous studies have proven that the orbit maneuver must change the angle measurement generated by the original trajectory recurrence to render the navigation problem observable [19,21].

Figure 1 shows how the pseudorange measurement is established. Let initial state vector be $\boldsymbol{x}_0 = \begin{bmatrix} \boldsymbol{r}_0^T & \boldsymbol{v}_0^T \end{bmatrix}^T$. Let nominal state vector $\bar{\boldsymbol{x}}(t) = \begin{bmatrix} \bar{\boldsymbol{r}}_t^T & \bar{\boldsymbol{v}}_t^T \end{bmatrix}^T$ contain the relative position and velocity when $\boldsymbol{u} = 0$ in Equation (1). Let actual state vector $\boldsymbol{x}(t) = \begin{bmatrix} \boldsymbol{r}_t^T & \boldsymbol{v}_t^T \end{bmatrix}^T$ contain the relative position and velocity when $\boldsymbol{u} \neq 0$ in Equation (1). In addition, $\delta\boldsymbol{r}_t$ represents the position disturbance due to impulse maneuver $\boldsymbol{u}$:

$$\delta\boldsymbol{r}_t = \boldsymbol{r}_t - \bar{\boldsymbol{r}}_t. \tag{3}$$
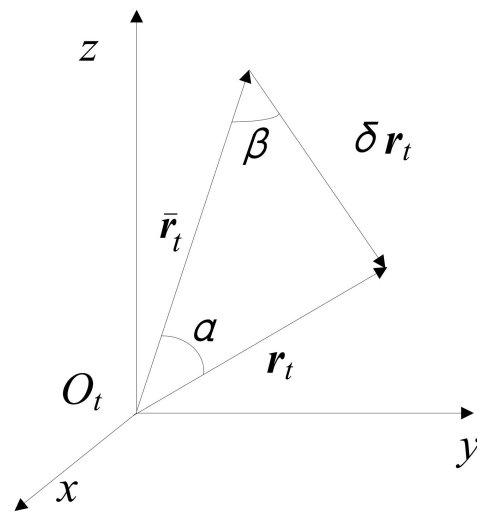
Figure 1. Geometric interpretation of a pseudorange measurement.

Then, the nominal line of sight $\bar{\boldsymbol{i}}_r$ and the actual line of sight $\boldsymbol{i}_r$ can be defined in Equations (4) and (5), respectively, as follows:

$$\bar{\boldsymbol{i}}_r = \frac{\bar{\boldsymbol{r}}_t}{|\bar{\boldsymbol{r}}_t|} = \frac{\boldsymbol{\Phi}_{rr}\boldsymbol{r}_0 + \boldsymbol{\Phi}_{rv}\boldsymbol{v}_0}{|\boldsymbol{\Phi}_{rr}\boldsymbol{r}_0 + \boldsymbol{\Phi}_{rv}\boldsymbol{v}_0|}, \tag{4}$$

$$\boldsymbol{i}_r = \frac{\boldsymbol{r}_t}{|\boldsymbol{r}_t|} = \frac{\boldsymbol{\Phi}_{rr}\boldsymbol{r}_0 + \boldsymbol{\Phi}_{rv}\boldsymbol{v}_0 + \boldsymbol{\Phi}_{rv}\boldsymbol{u}}{|\boldsymbol{\Phi}_{rr}\boldsymbol{r}_0 + \boldsymbol{\Phi}_{rv}\boldsymbol{v}_0 + \boldsymbol{\Phi}_{rv}\boldsymbol{u}|}, \tag{5}$$

where $\boldsymbol{\Phi}_{rr}$ and $\boldsymbol{\Phi}_{rv}$ are the subblocks in the block matrix form of $\boldsymbol{\Phi}$ and $\mathbf{G}$ that are defined in Appendix B.

Two angles are defined: observation angle α and disturbance angle β. Observation angle α is the angle between the actual line of sight $\boldsymbol{i}_r$ and the nominal line of sight $\bar{\boldsymbol{i}}_r$, and disturbance angle β is the angle between the nominal line of sight $\bar{\boldsymbol{i}}_r$ and position disturbance $\delta\boldsymbol{r}_t$, that is,

$$\alpha = \cos^{-1}(\bar{\boldsymbol{i}}_r \cdot \boldsymbol{i}_r) \quad \beta = \cos^{-1}\left(-\bar{\boldsymbol{i}}_r \cdot \frac{\delta\boldsymbol{r}_t}{|\delta\boldsymbol{r}_t|}\right). \tag{6}$$

If impulse maneuver $\boldsymbol{u}$ is known, position disturbance $\delta\boldsymbol{r}_t$ can be calculated as:

$$\delta\boldsymbol{r}_t = \boldsymbol{\Phi}_{rv}\boldsymbol{u}. \tag{7}$$

Then, observation angle α and disturbance angle β can be calculated. Using the sine theorem, under the ideal assumption of no angle measurement noise and no maneuver error, the distance at time t can be calculated as:

$$\rho = |\boldsymbol{r}_t| = |\delta\boldsymbol{r}_t| \cdot \frac{\sin\beta}{\sin\alpha}. \tag{8}$$

As shown in Figure 2, it is assumed that the pseudorange measurement error is caused by the angle measurement error and other factors, such as the orbit maneuver error, are not considered. References [20,24] analyzed the relationship between the pseudorange measurement error and the angle measurement error. Assuming that the angle measurement error is $\sigma_{\theta,\phi} \ll 1$, the resulting pseudo distance measurement error can be calculated as:

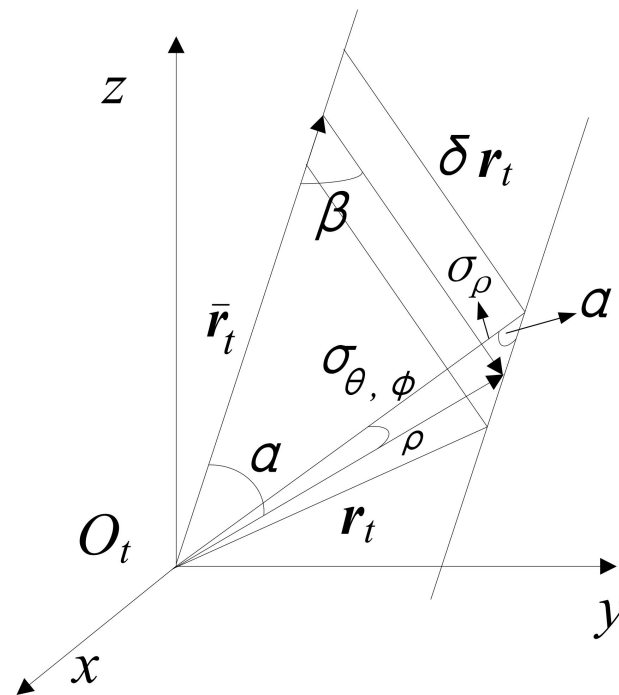$$\sigma_\rho \approx \sigma_{\theta,\phi} \cdot \frac{\rho}{\tan\alpha}. \tag{9}$$

Figure 2. Pseudorange measurement error caused by the angle measurement error.

In this way, measurement noise matrix R of AON based on the orbital maneuver can be obtained as:

$$R = \begin{bmatrix} \sigma_{\theta,\phi}^2 & 0 & 0 \\ 0 & \sigma_{\theta,\phi}^2 & 0 \\ 0 & 0 & \sigma_{\theta,\phi}^2 (\rho/\tan\alpha)^2 \end{bmatrix}. \tag{10}$$

2.3. Navigation Accuracy Estimation Based on the FIM and the CRLB

However, for AON, some observability criteria are proposed from the geometric interpretation or linear irrelevant theory, which are essential navigation accuracy criteria. For more extensive-state optimal estimation and filter design analysis, the FIM is a more general tool. The inverse of the FIM is the CRLB, which can be used to calculate the best estimation accuracy that can be obtained in unbiased estimation. Therefore, the CRLB is often used to calculate the best estimation accuracy that can be theoretically achieved. This paper uses the inverse of the FIM, namely, the CRLB, as the estimation criteria of navigation accuracy, which is also a part of the objective function of optimization as discussed in Section 4.

When new observations are obtained at time $k + 1$, the update of the FIM can be described by the following equation:

$$\mathbf{F}_{k+1} = \left[\left(\mathbf{\Phi}_{k+1}^T \right) \mathbf{F}_k^{-1} \mathbf{\Phi}_{k+1} + \mathbf{Q}_{k+1} \right]^{-1} + \mathbf{H}_{k+1}^T \mathbf{R}_{k+1}^{-1} \mathbf{H}_{k+1}, \tag{11}$$

where $\mathbf{F}_k \in R^{6\times6}$ represents the FIM at current time k, $\mathbf{F}_{k+1} \in R^{6\times6}$ represents the FIM after the new observation is obtained at time $k + 1$, $\mathbf{\Phi}_{k+1}$ is the state transition matrix from time k to time $k + 1$, $\mathbf{R}_{k+1}$ is the measurement noise with a pseudorange, $\mathbf{H}_k = \partial \mathrm{h}(\mathrm{x}_k)/\mathrm{x}_k$ represents the measurement sensitivity matrix with a pseudorange, and $\mathbf{Q}_{k+1}$ represents the process noise covariance matrix, which is used to describe the unmodeled error of the state transition equation.

The well-known CRLB can be obtained by calculating the inverse matrix of the FIM:

$$\mathbf{C}_k = \mathbf{F}_k^{-1}. \tag{12}$$

For the traditional angle-only measurement equations, the pseudorange measurement is not included explicitly, and the observation sensitivity matrix of the traditional angle-only measurement equations does not include the pseudorange information. Therefore, the traditional angle-only measurement equations are not directly applicable to the FIM calculation, unless the relative distance has been perfectly determined by the initial orbit determination and the initial state error can be modeled as zero-mean Gaussian white noise. The traditional angle-only observation equation has no observation ability to distinguish distance ambiguity; thus, the estimation of distance of the whole estimation process depends on the initial state with error. When the initial state error is no longer zero-mean Gaussian white noise, such an observation equation and an observation sensitivity matrix can also be calculated by the FIM and the CRLB, which can also converge, but the calculated FIM and CRLB cannot reflect the real estimation accuracy. The CRLB gives the lower bound of the estimation error, but in fact, the estimation error will be much larger than the CRLB, which goes against our original intention of using the CRLB to characterize the accuracy of state estimation. Therefore, this paper introduces the pseudorange measurement to the observation equation, observation sensitivity matrix, and measurement noise matrix to calculate the FIM and the CRLB.

3. Multipulse Glideslope Guidance

A multipulse glideslope approach trajectory is shown in Figure 3. The spacecraft is required to arrive at r_T in a fixed approach time T with a specified velocity v_T from the initial r_0 and v_0. Then, a straight line from r_0 to r_T denoted by the vector d is defined as the approach direction of the multipulse glideslope. At any instant in time, d can be expressed as $d(t) = r_T - r(t) = d i_d$, where d and i_d are the magnitude and unit direction of vector d, respectively, and i_d can be calculated as:
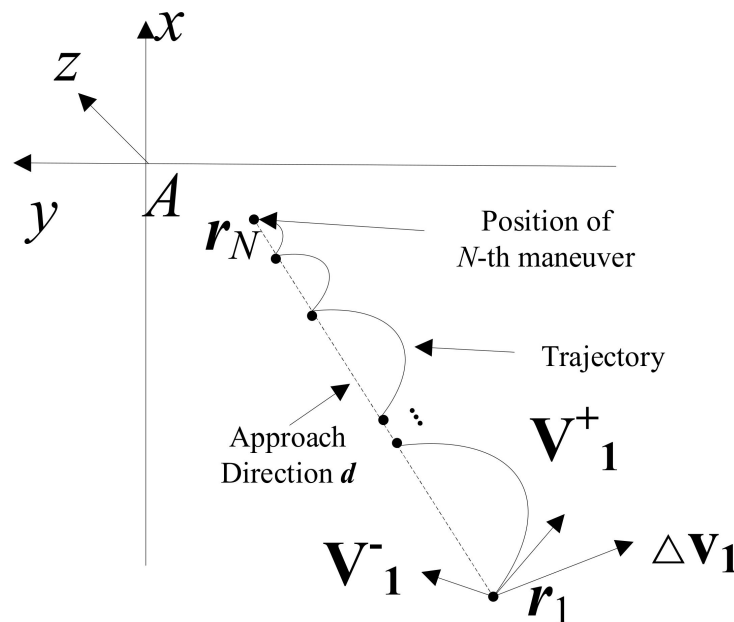
$$i_d = \frac{r_T - r_0}{|r_T - r_0|}. \tag{13}$$

Figure 3. An example of the multipulse glideslope approach trajectory.

The following linear relationship between d and its derivative $\dot{d}$ is adopted to ensure that the approach velocity decreases when the spacecraft approaches the target, shown as following:

$$\dot{d} = ad + b, \tag{14}$$

where a and b are constants that can be determined after the boundary conditions for d and its derivative $\dot{d}$ at $t = 0$ and $t = T$ are substituted as:

$$\text{for } t = 0, \ d = d_0 = |\boldsymbol{r}_T - \boldsymbol{r}_0|, \ \dot{d} = \dot{d}_0 < 0, \tag{15}$$

$$\text{for } t = T, \ d = d_T = 0, \ \dot{d} = \dot{d}_T < 0. \tag{16}$$

The solution to d has forms such as:

$$d(t) = c_1 e^{c_2 t} + c_3, \tag{17}$$

$$\dot{d}(t) = c_1 c_2 e^{c_2 t}, \tag{18}$$

where c_1, c_2, and c_3 are three constants of integration that can be determined after the boundary conditions. Then,

$$\begin{cases} d_0 = c_1 + c_3 \\ \dot{d}_0 = c_1 \cdot c_2 \\ d_T = c_1 e^{c_2 T} + c_3 \\ \dot{d}_T = c_1 c_2 e^{c_2 T} \end{cases}. \tag{19}$$

In addition, c_2 can be obtained first by numerically solving the following equation:

$$\dot{d}_0 e^{c_2 T} + c_2 d_0 - \dot{d}_0 = 0, \tag{20}$$

giving:

$$\begin{cases} c_1 = c_2 / \dot{d}_0 \\ c_3 = d_0 - c_1 \\ \dot{d}_T = \dot{d}_0 e^{c_2 T} \end{cases}. \tag{21}$$

Note that if $\dot{d}_0$ is known, $\dot{d}_T$ can also be determined.

A total of N pulses are applied during the whole approach process to divide the actual trajectory into $N - 1$ segments. Assuming that the time of applying pulses is $t_{dv}(i)$, $i = 1, 2, \cdots, N$, where $t_{dv}(1) = 0$ and $t_{dv}(N) = T$, the duration of each segment of the trajectory is $\Delta t_j = t_{dv}(j+1) - t_{dv}(j)$, $j = 1, 2, \cdots, N - 1$. After the last pulse is applied, the spacecraft reaches the target point that meets the velocity and position constraints.

Because the approaching trajectory is relatively far from the small body and the gravitational force of a small body is weak, we consider only the gravitational force of the Sun and ignore the gravitational force and other perturbation forces of the small body in the far approach phase. If the initial and terminal position vectors of the spacecraft relative to the asteroid are $\boldsymbol{r}_1 = \boldsymbol{r}_0$ and $\boldsymbol{r}_N = \boldsymbol{r}_T$, respectively, the i-th maneuver position $\boldsymbol{r}_i$ and time instant t_i of each impulse maneuver in the process of glideslope guidance are written as:

$$\begin{cases} \boldsymbol{r}_i = \boldsymbol{r}_T - \boldsymbol{d}_i = \boldsymbol{r}_T - d_i \boldsymbol{i}_d \\ t_i = t_{dv}(i) \end{cases}, \ i = 1, 2, \cdots, N, \tag{22}$$

where $d_i = d(t_i)$ represents the relative distance of the spacecraft from the terminal position at time instant t_i, which can be calculated using Equation (17).

The relative distance changes exponentially with time. The velocities v_i^- and v_i^+, $i = 1, 2, \cdots, N - 1$, before and after impulse maneuver $d\boldsymbol{v}_i$ at time instant t_i can be expressed as:

$$\begin{cases} \boldsymbol{v}_i^+ = \boldsymbol{\Phi}_{rv}^{-1}(t_{i+1}, t_i)(\boldsymbol{r}_{i+1} - \boldsymbol{\Phi}_{rr}(t_{i+1}, t_i)\boldsymbol{r}_i) \\ \boldsymbol{v}_{i+1}^- = \boldsymbol{\Phi}_{rv}(t_{i+1}, t_i)\boldsymbol{r}_i + \boldsymbol{\Phi}_{vv}(t_{i+1}, t_i)\boldsymbol{v}_i^+ \end{cases}, \tag{23}$$

where $\boldsymbol{\Phi}_{rr}(t_{i+1}, t_i)$, $\boldsymbol{\Phi}_{rv}(t_{i+1}, t_i)$, and $\boldsymbol{\Phi}_{vv}(t_{i+1}, t_i)$ are different blocks in the block form of the state transition matrix defined in Appendix B. According to the initial state and the terminal target state, the following equations can be obtained:

$$\begin{cases} \boldsymbol{v}_1^- = \boldsymbol{v}_0 \\ \boldsymbol{v}_N^+ = \boldsymbol{v}_T \end{cases}. \tag{24}$$

Then, the i-th ($i = 1, 2, \cdots, N$) maneuver $d\boldsymbol{v}_i$ at time instant t_i can be calculated as follows:

$$d\boldsymbol{v}_i = \boldsymbol{v}_i^+ - \boldsymbol{v}_i^-. \tag{25}$$

4. Navigation Accuracy-Enhanced Multipulse Glideslope Guidance Method

Multipulse guidance optimization often selects a set of control variables as the optimization variables, designs an optimization objective function and obtains the optimal trajectory under a specific standard after solving the optimization problem. For approach rendezvous guidance, components of multi-impulse maneuvers are often selected as the optimization variable, and the optimization object is the time or fuel. At the same time, constraints such as the approach corridor, maneuver amplitude, direction constraints, communication window, and target lighting are considered, and the rendezvous time is taken as a variable of the overall task design. Therefore, the optimal guidance problem is often a fuel optimization problem under fixed time and multiple constraints.

As mentioned above, when approaching an asteroid from afar, only AON can be used, so observability or navigation accuracy must be considered. In addition, the target characteristics of asteroids are highly unknown, so the target illumination, that is, the solar phase angle, becomes particularly important for autonomous rendezvous trajectory design. The multipulse glideslope guidance method has natural advantages in approaching a target from a fixed direction. With the distance approaching, the approach velocity also decreases, and the degree of safety is high. The approach trajectory of multipulse glideslope guidance has natural geometric constraints, that is, approaching a small celestial body from a fixed direction. When the number of pulses is fixed, the maneuver can be calculated according to the initial state, terminal state, total approach time, pulse maneuver time, and initial approach velocity.

4.1. Problem Description

The asteroid far-approach phase starts from asteroid capture by the camera, and the initial relative state is calculated from the inertial position and velocity of the spacecraft based on measurement and control and the ephemeris of the small body. The terminal rendezvous time and terminal aiming relative state are established by the overall mission design. This phase also requires less fuel consumption to approach the target point. Therefore, this paper constructs the following asteroid approach problem:

Given initial relative state $\bar{\boldsymbol{x}}_0$ and terminal aiming relative state $\bar{\boldsymbol{x}}_f$ (overall task design), the fixed terminal time t_f (overall task design), the fixed total number of orbital maneuvers N, the first maneuver time $t_1 = t_0$, and the last maneuver time $t_N = t_f$, with initial relative distance change rate $\dot{d}_0$ and maneuver time $t_i = t_{dv}(i)$, $i = 2, \cdots, N-1$ as variables, a nonlinear programming problem to optimize the FIM-based navigation accuracy object and fuel consumption object is developed.

4.2. Fuel Consumption Objective

Far-approach rendezvous generally requires the optimization of fuel consumption. The fuel consumption function can be formalized as the sum of the magnitude of all maneuvers during the approach phase, which can be shown as:

$$J_f = \sum_{i=1}^{N} |d\boldsymbol{v}_i|, \tag{26}$$

where dv_i is the *i*-th maneuver at time instant t_i and $|\cdot|$ is the 2-norm operator.

4.3. Navigation Error Objective

The navigation error objective function is constructed as:

$$J_o = \sum_{i=1}^{N_o} \sum_{j=1}^{3} C_i(j,j) / \|\boldsymbol{r}_i\|_2^2, \tag{27}$$

where N_o is the total number of observations, $C_i(j,j)$ is the j-th diagonal element of the CRLB matrix, and $\|\boldsymbol{r}_i\|_2$ is the relative distance at the observation time. The diagonal elements of the CRLB matrix reflect the estimation accuracy of the corresponding system state. The smaller the navigation error objective J_o, the better the navigation accuracy.

4.4. Optimization Objectives

Multiobjective optimization seeks a balanced compromise between multiple optimal objectives. Therefore, there is no unique optimal solution, but rather a Pareto optimal solution set. The improvement of solutions in this solution set on one goal is at the cost of reducing another goal. A simple processing method is to design the optimization objective as the weighted sum of multiple objectives, that is, the weighted sum of the navigation accuracy object and fuel consumption:

$$J_w = (1-w)J_f + wJ_o, \tag{28}$$

where w is the weight of a navigation accuracy objective, with the range of $[0,1]$, $w = 0$ represents the domination of the fuel consumption objective, and $w = 1$ represents the domination of the navigation error objective.

4.5. Constraints

In an actual mission, certain preparations, such as attitude adjustment, are required before a spacecraft orbit maneuver. Therefore, the maneuver time needs to meet the constraints of the minimum maneuver time interval τ, which can be written as:

$$t_i > t_{i-1} + \tau, \; i = 2, 3, \cdots, N. \tag{29}$$

4.6. Optimization Problem

To generate the angle-only rendezvous trajectory with an optimal navigation accuracy and fuel consumption, Sections 4.2–4.5 can be summarized in the form of the following optimization problem:

$$\begin{aligned} &\min_{Y} J_w \\ &\text{subject to } t_i > t_{i-1} + \tau, \; i = 2, 3, \cdots, N \end{aligned} \tag{30}$$

Optimal solution Y_{opt} is the optimal maneuver time $t_i = t_{dv}^*(i)$, $i = 2, \cdots, N-1$, and the initial relative distance change rate is $\dot{d}_0^*$, which can be substituted into the multipulse glideslope guidance to obtain the corresponding maneuver amplitude and direction at each maneuver time.

Under a certain objective weight w, the above optimization problem can be solved using standard optimization algorithms such as the interior point method. This is the offline multipulse glideslope guidance method with an enhanced navigation accuracy.

5. Numerical Simulation

5.1. Simulation Conditions

Taking 2016HO3 as the object asteroid (see Table 1 for its orbital elements), a simulation study of multipulse glideslope guidance with an enhanced navigation accuracy for the

far approach offline was carried out. The start time of the approach rendezvous is shown in Table 2. According to the transfer scheme, it is planned to approach from 100,000 km to 100 km from the asteroid by 6 impulse maneuvers. Table 2 summarizes the simulation parameters used. To verify the effectiveness of the proposed method, different values of the tradeoff weight w between the navigation error objective and the fuel consumption objective were used for Monte Carlo simulation. Each value of the tradeoff weight w was simulated 100 times, and the statistics were analyzed.

Table 1. Orbit elements of 2016HO3.

Epoch 2459600.5 (2022-Jan-21.0) TDB Reference: Heliocentric J2000 Ecliptic		
Element	**Value**	**Units**
Semimajor axis	1.001137344063433	AU
Eccentricity	0.1029843787386461	
Inclination	7.788928644671124	deg
Longitude of the ascending node	66.0142959682462	deg
Perihelion argument angle	305.6646720090911	deg
Mean anomaly	107.172338605596	deg

Table 2. Simulation parameters.

Parameter	Value	Unit
Environment		
Equivalent disturbance 1σ	1×10^{-8}	m/s^2
Equivalent disturbance 1σ	1	mrad
Sample time	10	s
Rendezvous Mission		
Initial condition $x_0 = [x, y, z, \dot{x}, \dot{y}, \dot{z}]$	$[0, -99160, -7490, -0.068, 0.458, 0.036]$	km km km km/s km/s km/s
Target condition $x_f = [x, y, z, \dot{x}, \dot{y}, \dot{z}]$	$[14, -100, 0, 0, 0, 0]$	km km km km/s km/s km/s
Number of pulses N	6	
Start time t_0	2023-May-7	
Total time T	15.5	day
Optimization Parameter		
Minimum maneuver interval time τ	5	hour
Navigation Initiation		
Initial navigation error 1σ	$[1000, 1000, 1000, 1, 1, 1]$	km km km km/s km/s km/s

5.2. Navigation Accuracy-Enhanced Multipulse Glideslope Guidance Optimum Results

w is the tradeoff weight of the fuel consumption objective and the navigation error objective. We conducted a parameter analysis of w to show its influence on the resulting optimal maneuvers and the resulting rendezvous trajectory. Different values of the tradeoff weight w were set to solve the optimization problem.

Figure 4 shows the resulting optimal trajectories corresponding to different tradeoff weights w. When w takes a larger value, such as $w = 0.5$ or 1.0, which means the navigation accuracy is more emphasized, the corresponding trajectories show less deviation from the direction of the approaching straight line after the first maneuver, and the maneuvers are distributed more evenly over relative distances. This result is opposite to the result in [18] in the context of the Vbar approach, because the mission condition in this paper is different with a large initial velocity. At the latter stage of trajectories, all trajectories seem alike, which can be distinguished in the following analysis.
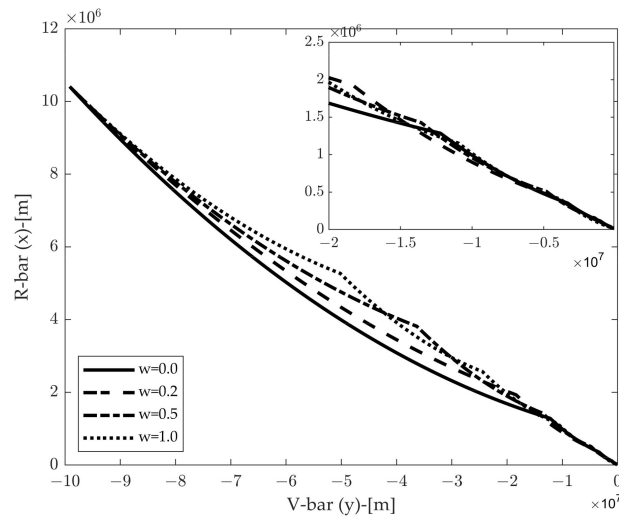
Figure 4. Resulting optimal trajectories corresponding to different tradeoff weights w.

Figure 5 shows the distributions of the magnitude of dvs along the optimal trajectories with different w. Overall, the maneuvers show a gradually decreasing trend over time, which verifies the safety benefit of the guidance method. When w takes a larger value, such as 0.5 or 1, the magnitude of the first maneuver is larger, and the magnitude of the second maneuver shows an opposite trend. The small magnitudes of the last two maneuvers with different w are consistent with the relatively small deviation seen at the latter stage of trajectories in Figure 4.
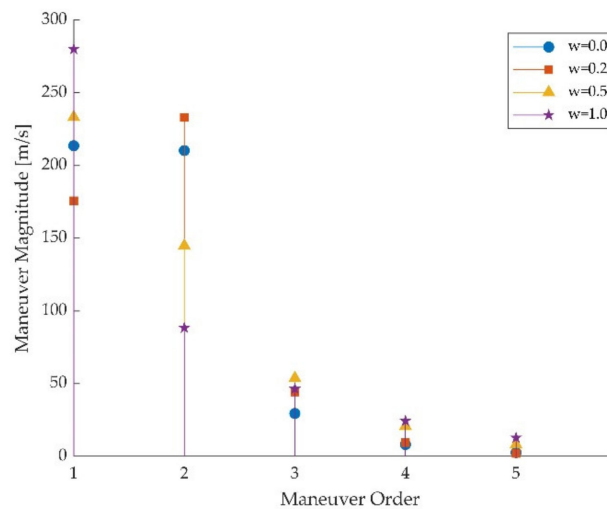
Figure 5. Distributions of the magnitude of dvs along the optimal trajectories with different w.

Figures 6 and 7 show how the fuel consumption (total Δv) and the navigation error objective of the resulting trajectories change with the tradeoff weight w. It is seen that with the increasing w, which means more emphasis is placed on the navigation error objective, the fuel consumption begins to increase and the navigation error objective begins to decrease when w is larger than 0.6, and the navigation error objective starts to play a major role. The tradeoff weight w must be at least 0.7 to bring obvious improvement in navigation accuracy at the cost of extra fuel consumption. A clearer correlation between the fuel consumption and the navigation error objective can be spotted from Figure 8, where these two quantities are plotted. The navigation accuracy continues to improve with the increasing fuel consumption.
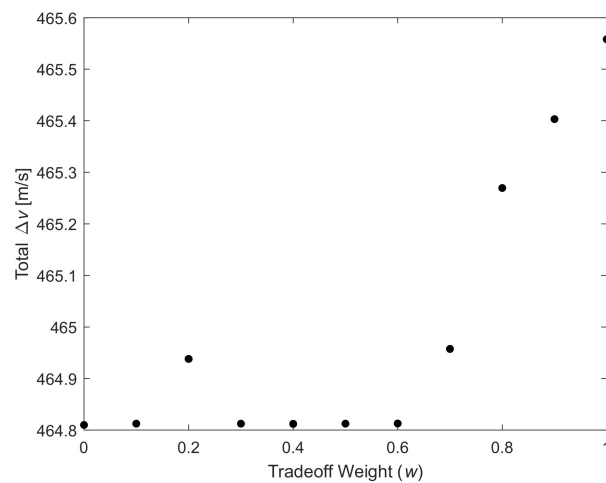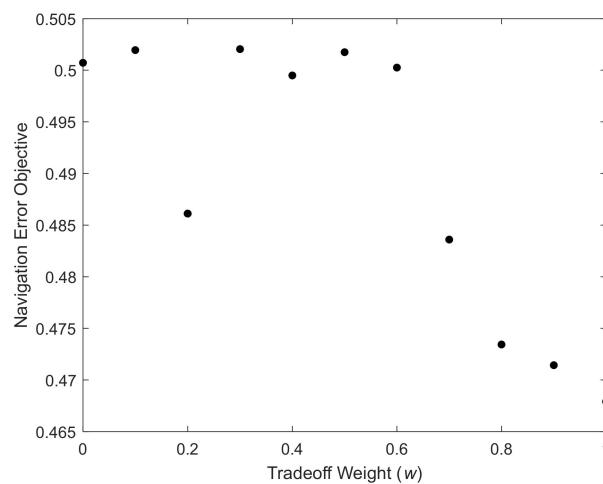
Figure 6. Fuel consumption vs. tradeoff weight.

Figure 7. Navigation error objective vs. tradeoff weight.
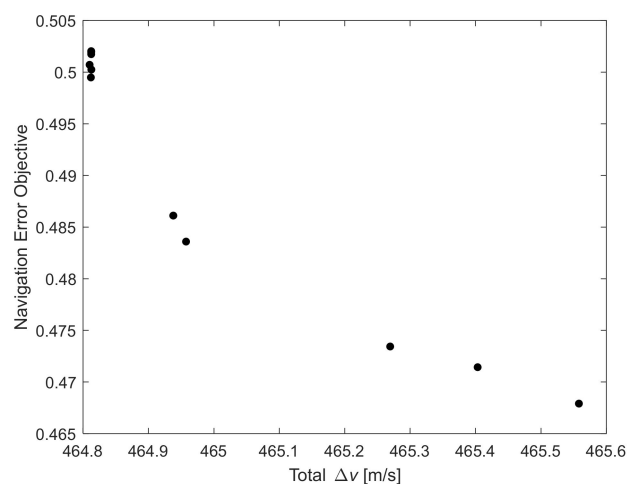

Figure 8. Navigation error objective vs. fuel cost.

Table 3 shows the distributions of the time instants of dvs along the optimal trajectories with different w. It can be seen that the distributions are similar, which indicates that the optimal distribution of the time instants of dvs remains stable and insensitive when w takes different values. However, as shown in Figure 9, the initial relative distance change rate decreases significantly, as w increases. This is attractive, because the optimal distribution

of the time instants of dvs can be solved only once and then fixed when the optimization problem has to be solved multiple times onboard with different w, which will leave initial relative distance change rate $\dot{d}_0$ as the only optimization variable. Although this will save the time of the optimization computation, it will lead to a satisfactory solution instead of an optimal solution.

Table 3. Distributions of the time instants of dv s along the optimal trajectories with different w.

Tradeoff Weight	Maneuver Time Instant (/T)			
w	2nd Maneuver	3rd Maneuver	4th Maneuver	5th Maneuver
0	0.260	0.424	0.575	0.739
0.1	0.263	0.425	0.574	0.736
0.2	0.268	0.427	0.572	0.731
0.3	0.263	0.425	0.574	0.736
0.4	0.262	0.425	0.574	0.737
0.5	0.264	0.426	0.573	0.735
0.6	0.264	0.425	0.574	0.735
0.7	0.257	0.422	0.577	0.742
0.8	0.230	0.411	0.588	0.769
0.9	0.263	0.425	0.574	0.736
1	0.257	0.422	0.577	0.742
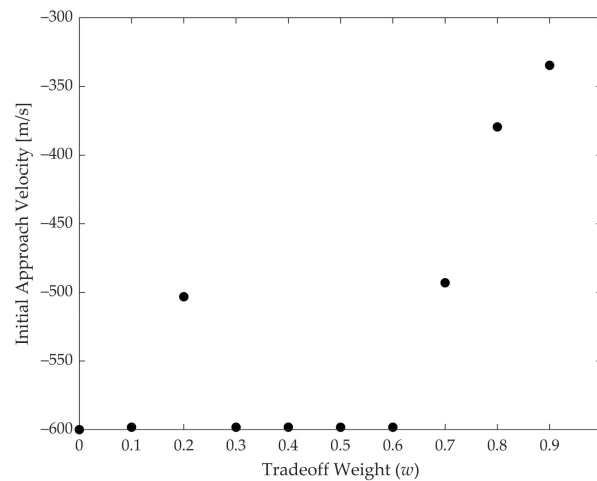
Figure 9. Initial approaching speed vs. tradeoff weight.

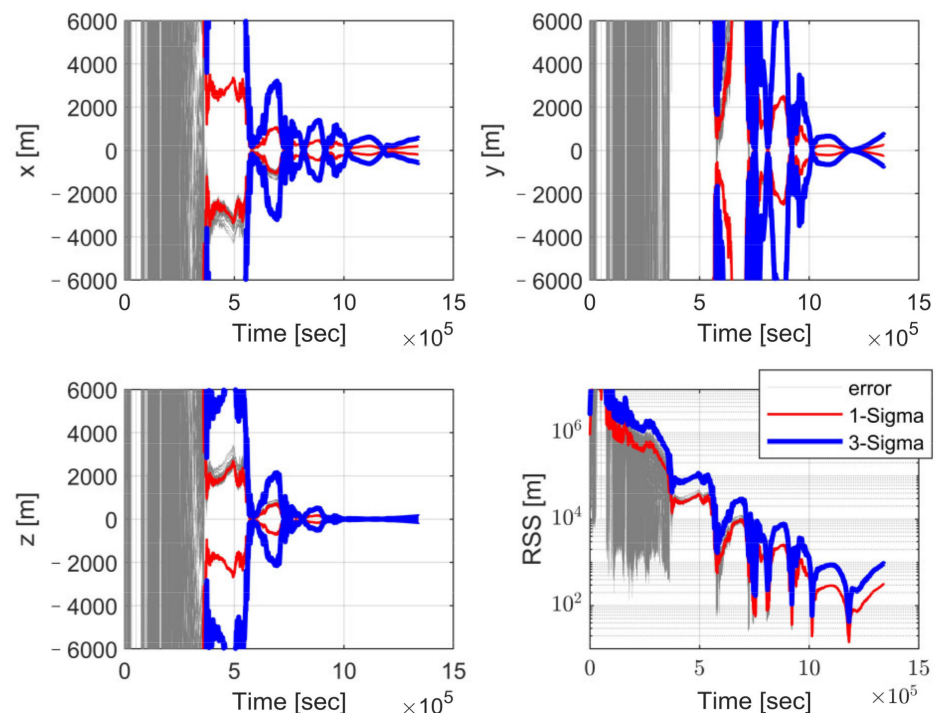### 5.3. AON Using Resulting Trajectories

To verify that the proposed guidance strategy can improve the performance of AON, an AON simulation model is constructed, as shown in Figure 10. Navigation filtering [30] is based on the classical Cartesian extended Kalman filter (EKF) and TH equations. The calculated maneuver is directly input into the dynamic model of the spacecraft, regardless of the realization model and the control error of the maneuver.
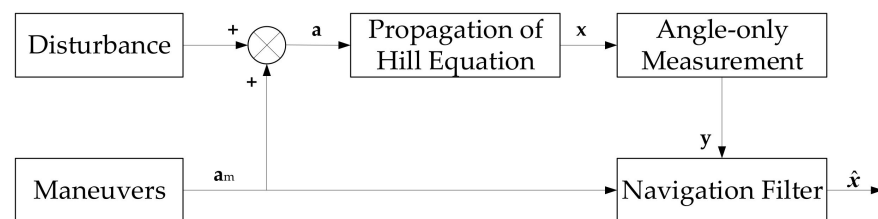
Figure 10. Simulation model of angle-only navigation using resulting approach maneuvers.

The Monte Carlo simulation for each w includes 100 realizations of truth trajectories and the associated set of angle-only observables generated in each realization. In each realization, the filter model is the EKF, starts with the same nominal reference trajectory and processes the data from the realization. For the case of $w = 0.3$, the state position errors and the associated uncertainties in each position component and associated RSS (residual sum of squares) are presented in Figure 11. Shown are the 1-sigma and 3-sigma uncertainty bounds as well as the filter solution error obtained by differencing the filter solutions with the truth trajectory. Additionally, listed in the results are statistics of the percentage by which a filter solution exceeds the 1-sigma and the 3-sigma uncertainty bounds. In the present case, the respective percentages are 28.463% and 0.002%, from a population of 13,392,200 samples. Assuming ergodic processes and statistics that conform to a normal distribution, one expects 1-sigma exceedances to be <31.7% of the time and 3-sigma exceedances to be <0.3% of the time, which is true for this case. For the case of $w = 0.3$, the state velocity errors and the associated uncertainties in each velocity component and the associated RSS (in the lower right) are presented in Figure 12. The statistics of the percentage at which a filter solution exceeds the 1-sigma and 3-sigma bounds show that the filter works normally, which are 28.670% and 0.007%, respectively. Because of the dispersion of initial navigation errors, the dispersion of the navigation errors is still obvious at the early stage of the trajectory, but it then reduces significantly. Another observation with these results is that as the spacecraft is close to the asteroid, the navigation errors fluctuate with the maneuvers, because after each maneuver, it takes some time for the AON filter to converge when the magnitude of the maneuver is relatively small at the latter stage of the trajectory.


Figure 11. Angle-only navigation position errors along the resulting trajectory for 100 realizations and uncertainties (1-sigma uncertainty bound in red and 3-sigma uncertainty bound in blue) for the case with $w = 0.3$.

w=0.3, Velocity Error Statistic: 25.7139% Outside 1-sig, 0.013814% Outside 3-sig, (population = 13392100 from 100 realizations).
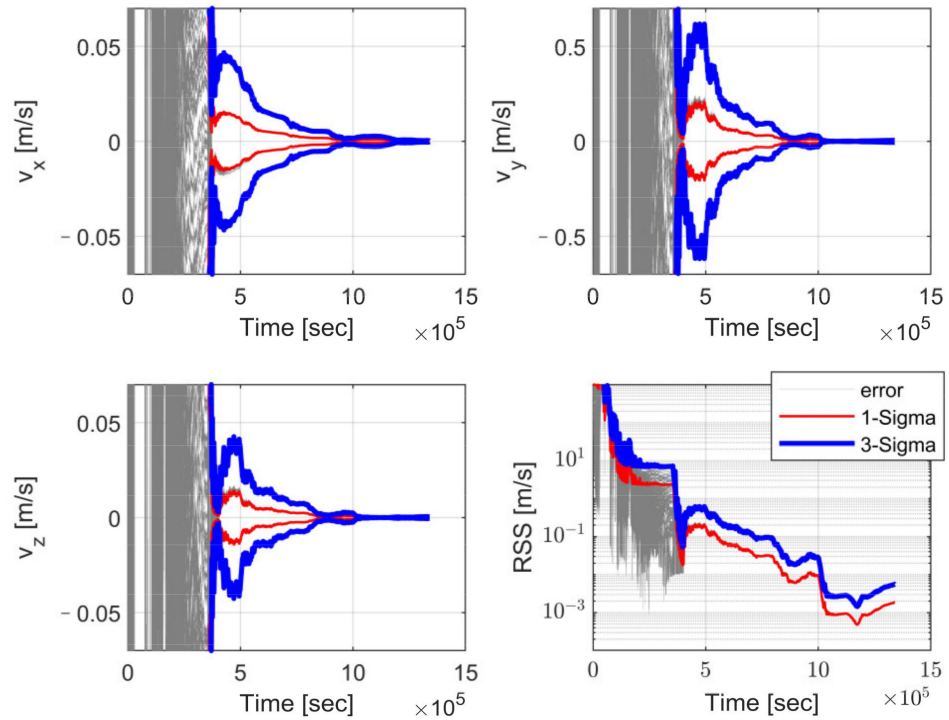
Figure 12. Angle-only navigation velocity errors along the resulting trajectory for 100 realizations and uncertainties (1-sigma uncertainty bound in red and 3-sigma uncertainty bound in blue) for the case with $w = 0.3$.

As shown in Figure 13, when the tradeoff weight w increases, the navigation error converges faster first, but the navigation error then increases. In spacecraft rendezvous, there is a quantified minimum navigation accuracy rule, the 1% range rule, which is that the relative navigation accuracy needs to be guaranteed to be at least 1% of the relative distance [23]. Figure 14 shows that along the trajectory, the navigation error converges to less than 1% of the range.
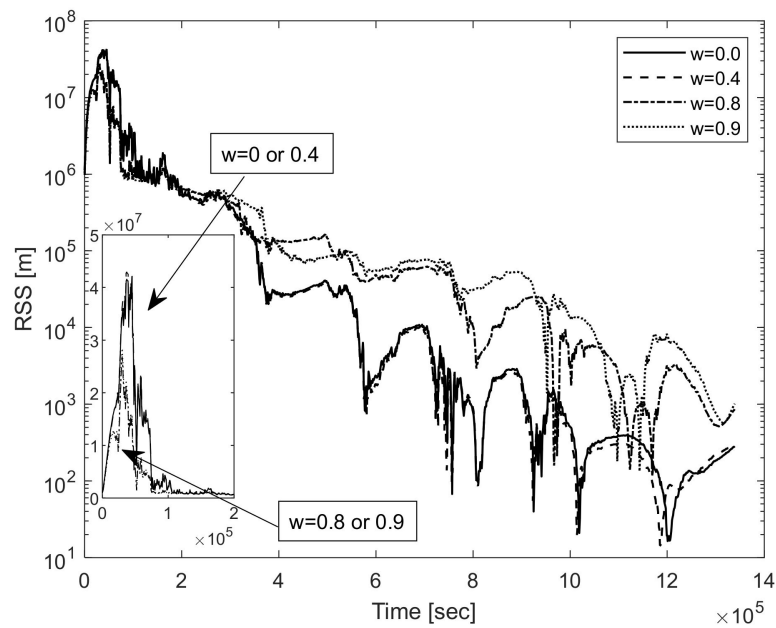
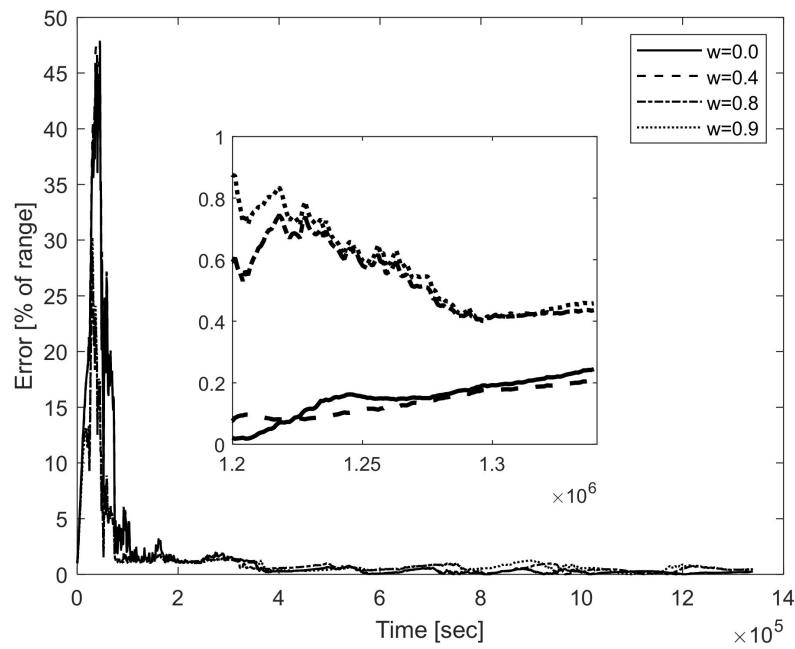**Figure 13.** Sample navigation errors for typical tradeoff weights.

Figure 14. Sample navigation errors (% of range) for typical tradeoff weights.

As shown in Figure 15, with the increasing tradeoff weight w, the whole navigation error decreases gradually. Tradeoff weight w should be at least 0.7 to see a clear effect. Similarly, Figure 16 shows that the reduction in the whole-range navigation error comes at the cost of increased fuel consumption. As shown in Figures 17 and 18, the arrival navigation error and the whole navigation error show the opposite trend. With the increasing tradeoff weight w and fuel consumption, the arrival navigation error also shows an increasing trend. Therefore, to improve the navigation accuracy at the time of arrival, less fuel can be used; that is, tradeoff weight w can be 0, corresponding to fuel optimal guidance. This shows that the navigation error in the early stage of the approach phase and the navigation error in the later stage or the final arrival navigation error are subject to mutual compromise, which is very important.
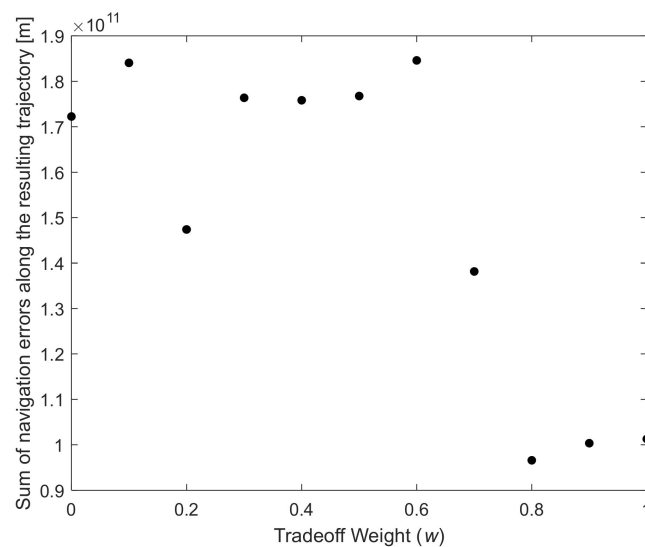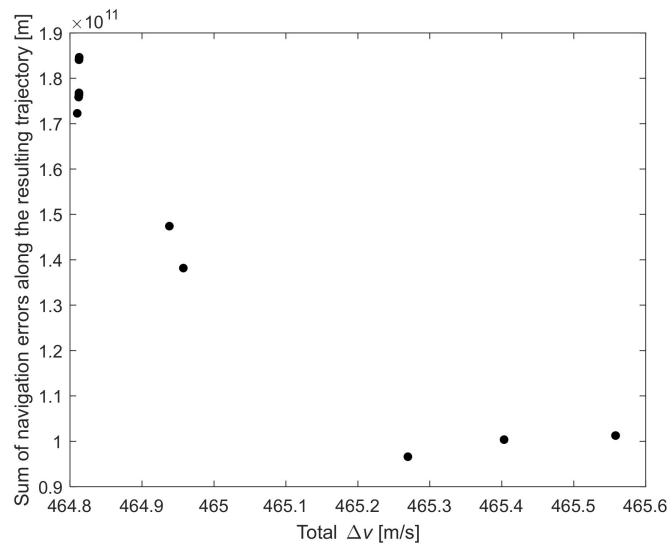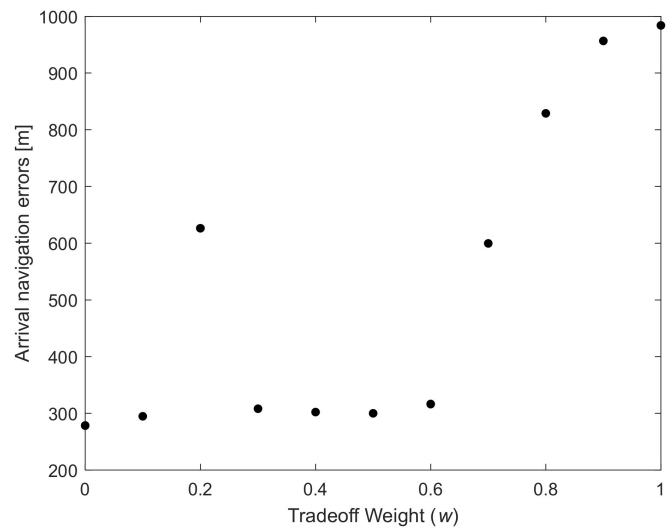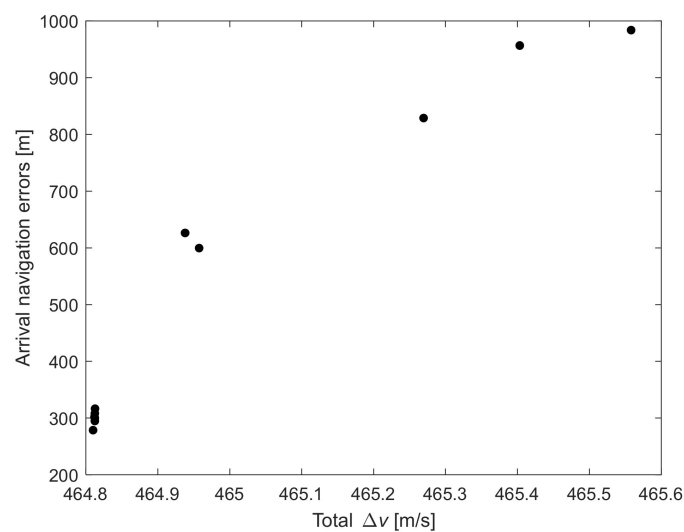

Figure 15. Sum of navigation errors along the resulting trajectory vs. tradeoff weight w.

Figure 16. Sum of navigation errors along the resulting trajectory vs. fuel cost.

Figure 17. Arrival navigation error vs. tradeoff weight *w*.

Figure 18. Arrival navigation error vs. fuel cost.

6. Conclusions

This paper proposes a navigation accuracy-enhanced glideslope guidance method in the context of bearing-only navigation. The tradeoff between the navigation accuracy and the fuel consumption was deeply numerically analyzed. Navigation accuracy can be improved at the cost of extra fuel consumption. The trade-off factor between the navigation accuracy and the fuel consumption has little effect on the pulse maneuver conduction time corresponding to the optimal solution, so the optimal pulse maneuver conduction time can be fixed in engineering implementation. However, the trade-off factor has a very direct impact on the initial relative distance change rate. There is a strong correlation between the navigation accuracy and the fuel consumption trade-off factor, initial relative distance change rate, total fuel consumption, initial maneuver, and navigation accuracy. Therefore, during project implementation, one variable can be changed to change another variable. For example, we can fix the maneuver pulse time and take the change rate of the initial relative distance as the only optimization variable to improve the optimization problem-solving speed. This is attractive for using this method in online closed-loop guidance. The proposed method retains the advantages of a multipulse glideslope guidance method; for example, the approach direction can be designed on demand, and the approach speed decreases with the distance. All these contributions provide a reference for the rendezvous trajectory design of high-precision AON and the design of an autonomous guidance algorithm for the far approach phase of angle-only rendezvous missions.

Institutional Review Board Statement: Not applicable.

Informed Consent Statement: Not applicable.

Data Availability Statement: Not applicable.

Appendix A. Asteroid Hill Rotation Reference Frame

To describe the relative motion between the spacecraft and the asteroid, the coordinate systems shown in Figure A1 are established, including the asteroid Hill rotation coordinate system $O_a xyz$ and the heliocentric inertial coordinate system $O_s XYZ$. The spacecraft and the asteroid can be regarded as points.

The center O_a is at the barycenter of the asteroid. $O_a xyz$ rotates at the orbital angular velocity ω relative to $O_s XYZ$. Its basic plane is the asteroid orbital plane, and $O_a xyz$ is defined as follows:

1. The x axis is inward along the orbit radius;
2. The z axis follows the angular momentum direction of the asteroid's orbit;
3. The y axis completes the right-handed coordinate system and is perpendicular to the x axis in the orbital plane.

The unit vector corresponding to the asteroid Hill rotation coordinate system $O_a xyz$ is $\{i_x, i_y, i_z\}$, and the unit vector corresponding to the heliocentric inertial coordinate system $O_s XYZ$ is $\{i_X, i_Y, i_Z\}$.
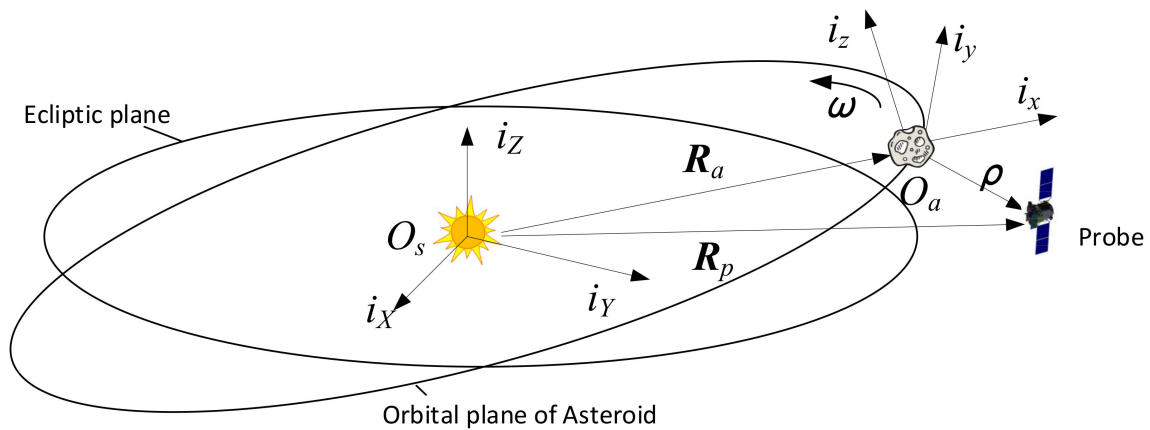
Figure A1. Definition of asteroid Hill rotation coordinate systems.

Appendix B. Tschauner–Hempel Equation of a Relative Motion

The relative motion between the spacecraft and the asteroid is shown in Figure A1. If the asteroid travels in an elliptical orbit around the Sun, the asteroid orbit in the heliocentric inertial system can be described by classical orbit elements, that is, the semimajor axis, eccentricity, inclination, longitude of the ascending node, perihelion argument angle, and true anomaly $(a, e, i, \Omega, \omega, f)$.

Therefore, the state transition matrix can be defined as:

$$\boldsymbol{\Phi}(f, f_0) = \begin{bmatrix} \boldsymbol{\Phi}_{rr}(f, f_0) & \boldsymbol{\Phi}_{rv}(f, f_0) \\ \boldsymbol{\Phi}_{vr}(f, f_0) & \boldsymbol{\Phi}_{vv}(f, f_0) \end{bmatrix}. \tag{A1}$$

For the specific details of $\boldsymbol{\Phi}(f, f_0)$, see [28]. The state transition matrix is transferred from the true anomaly frame to the time frame; then,

$$\boldsymbol{\Phi}_{rr}(t, t_0) = \{A_0 \boldsymbol{\Phi}_{rr}(f, f_0) + B_0 \boldsymbol{\Phi}_{rv}(f, f_0)\} / A, \tag{A2}$$

$$\boldsymbol{\Phi}_{rv}(t, t_0) = \{A_0 \boldsymbol{\Phi}_{rr}(f, f_0) + B_0 \boldsymbol{\Phi}_{rv}(f, f_0)\} / A, \tag{A3}$$

$$\boldsymbol{\Phi}_{vr}(t, t_0) = \{(A_0 \boldsymbol{\Phi}_{vr}(f, f_0) + B_0 \boldsymbol{\Phi}_{vv}(f, f_0)) \\ -B \boldsymbol{\Phi}_{rr}(t, t_0)\} / C \tag{A4}$$

$$\boldsymbol{\Phi}_{vv}(t, t_0) = \{C_0 \boldsymbol{\Phi}_{rv}(f, f_0) - B \boldsymbol{\Phi}_{rv}(t, t_0)\} / C, \tag{A5}$$

$$A = \frac{1 + ec_f}{a(1 - e^2)}, \quad B = \frac{-es_f}{a(1 - e^2)}, \quad C = \frac{A}{\dot{f}}. \tag{A6}$$

If $t_0 = 0$, then $\boldsymbol{\Phi}_{rr}(t, t_0)$, $\boldsymbol{\Phi}_{rv}(t, t_0)$, $\boldsymbol{\Phi}_{vr}(t, t_0)$, and $\boldsymbol{\Phi}_{vv}(t, t_0)$ can be abbreviated as $\boldsymbol{\Phi}_{rr}(t)$, $\boldsymbol{\Phi}_{rv}(t)$, $\boldsymbol{\Phi}_{vr}(t)$, and $\boldsymbol{\Phi}_{vv}(t)$, respectively. Then, Φ (t) can be described as:

$$\boldsymbol{\Phi}(t) = \begin{bmatrix} \boldsymbol{\Phi}_{rr}(t) & \boldsymbol{\Phi}_{rv}(t) \\ \boldsymbol{\Phi}_{vr}(t) & \boldsymbol{\Phi}_{vv}(t) \end{bmatrix}. \tag{A7}$$

The input matrix corresponding to the impulse maneuver at time t_0 is $G(t)$; then,

$$G(t) = \begin{bmatrix} \boldsymbol{\Phi}_{rv}(t) \\ \boldsymbol{\Phi}_{vv}(t) \end{bmatrix}. \tag{A8}$$

If dT is a sampling step, then,

$$\boldsymbol{\Phi}_{k+1} \equiv \boldsymbol{\Phi}(k+1, k) \equiv \boldsymbol{\Phi}((k+1) \cdot dT, k \cdot dT). \tag{A9}$$

Appendix C. Angle Measurement and Pseudodistance Measurement

The angle-only measurement equation based on the orbital maneuver includes the real measurement of the azimuth angle θ and the elevation angle ϕ of the spacecraft relative to the target asteroid and the pseudo measurement of distance d of the spacecraft relative to the target. These angles and distances are defined in the asteroid Hill rotation coordinate system, as shown in Figure A2. The azimuth angle θ is defined from $0°$ to $180°$, and the elevation angle ϕ is set to be from $-90°$ to $+90°$.
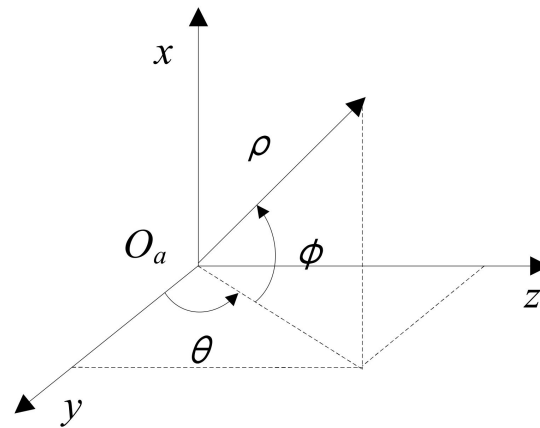
Figure A2. Measurement angle and relative distance of the asteroid in the asteroid Hill rotating reference frame.

References

1. Rivkin, A.S.; Chabot, N.L.; Stickle, A.M.; Thomas, C.A.; Richardson, D.C.; Barnouin, O.; Fahnestock, E.G.; Ernst, C.M.; Cheng, A.F.; Chesley, S.; et al. The Double Asteroid Redirection Test (DART): Planetary Defense Investigations and Requirements. *Planet. Sci. J.* **2021**, *2*, 173. [CrossRef]
2. Vaughan, R.; Riedel, J.; Davis, R.; Owen, J.W.; Synnott, S. Optical navigation for the Galileo Gaspra encounter. In Proceedings of the Astrodynamics Conference, Hilton Head Island, SC, USA, 10–12 August 1992; p. 4522.
3. Miller, J.K.; Williams, B.G.; Bollman, W.E.; Davis, R.P.; Yeomans, D.K. Navigation analysis for Eros rendezvous and orbital phases. *J. Astronaut. Sci.* **1995**, *43*, 453–476.
4. Broschart, S.; Bhaskaran, S.; Bellerose, J.; Dietrich, A.; Han, D.; Haw, R.; Mastrodemos, N.; Owen, W.M.; Rush, B.; Surovik, D. Shadow navigation support at jpl for the rosetta landing on comet 67p/churyumov-gerasimenko. In Proceedings of the 26th International Symposium on Space Flight Dynamics ISSFD, number ISSFD-2017-096, Matsuyama, Japan, 3–9 June 2017.
5. Kominato, T.; Matsuoka, M.; Uo, M.; Hashimoto, T.; Kawaguchi, J.I. Optical hybrid navigation and station keeping around Itokawa. In Proceedings of the AIAA/AAS Astrodynamics Specialist Conference and Exhibit, Keystone, Colorado, 21–24 August 2006; p. 6535.
6. Tsuda, Y.; Takeuchi, H.; Ogawa, N.; Ono, G.; Kikuchi, S.; Oki, Y.; Ishiguro, M.; Kuroda, D.; Urakawa, S.; Okumura, S.-I. Rendezvous to asteroid with highly uncertain ephemeris: Hayabusa2's Ryugu-approach operation result. *Astrodynamics* **2020**, *4*, 137–147. [CrossRef]
7. Lamey, Q.; Vance, L.D.; Thangavelautham, J. The Impact of the Yarkosvky Effect on Satellite Navigation around Small Bodies. *ASCEND 2021* **2021**, *2021*, 4173.
8. Yu, Z.; Shang, H.; Wei, B. Accessibility assessment and trajectory design for multiple Near-Earth-asteroids exploration using stand-alone CubeSats. *Aerosp. Sci. Technol.* **2021**, *118*, 106944. [CrossRef]
9. Gil-Fernandez, J.; Prieto-Llanos, T.; Cadenas-Gorgojo, R.; Graziano, M.; Drai, R. Autonomous GNC Algorithms for Rendezvous Missions to Near-Earth-Objects. In Proceedings of the AIAA/AAS Astrodynamics Specialist Conference & Exhibit, Honolulu, HI, USA, 18–21 August 2008.
10. Bhaskaran, S. Autonomous navigation for deep space missions. *SpaceOps 2012* **2012**, *2012*, 1267135.
11. Vetrisano, M.; Yarnoz, D.G.; Branco, J. Effective approach navigation prior to small body deflection. In Proceedings of the Space Generation Congress, Beijing, China, 23–27 September 2013.
12. Richards, A.; Feron, E.; How, J.P.; Schouwenaars, T. Spacecraft Trajectory Planning with Avoidance Constraints Using Mixed-Integer Linear Programming. *J. Guid. Control. Dyn.* **2002**, *25*, 755–764. [CrossRef]
13. Boyd, S.; Vandenberghe, L. *Convex Optimization*; Cambridge University Press: Cambridge, UK, 2004.
14. Weiss, A.; Baldwin, M.; Erwin, R.S.; Kolmanovsky, I. Model Predictive Control for Spacecraft Rendezvous and Docking: Strategies for Handling Constraints and Case Studies. *IEEE Trans. Control. Syst. Technol.* **2015**, *23*, 1638–1647. [CrossRef]
15. Hartley, E. A tutorial on model predictive control for spacecraft rendezvous. In Proceedings of the Control Conference, Osaka, Japan, 15–18 December 2015.

16. Hablani, H.B.; Tapper, M.L.; Dana-Bashian, D.J. Guidance and Relative Navigation for Autonomous Rendezvous in a Circular Orbit. *J. Guid. Control. Dyn.* **2002**, *25*, 553–562. [CrossRef]

17. Benedikter, B.; Zavoli, A. Convex Optimization of Linear Impulsive Rendezvous. *arXiv* **2019**, arXiv:1912.08038.

18. Grzymisch, J.; Fichter, W. Optimal Rendezvous Guidance with Enhanced Bearings-Only Observability. *J. Guid. Control. Dyn.* **2015**, *38*, 1131–1140. [CrossRef]

19. Woffinden, D.C.; Geller, D.K. Observability Criteria for Angles-Only Navigation. *IEEE Trans. Aerosp. Electron. Syst.* **2009**, *45*, 1194–1208. [CrossRef]

20. Woffinden, D.C.; Geller, D.K. Optimal Orbital Rendezvous Maneuvering for Angles-Only Navigation. *J. Guid. Control Dyn.* **2009**, *32*, 1382–1387. [CrossRef]

21. Grzymisch, J.; Fichter, W. Observability Criteria and Unobservable Maneuvers for In-Orbit Bearings-Only Navigation. *J. Guid. Control Dyn.* **2014**, *37*, 1250–1259. [CrossRef]

22. Grzymisch, J.; Fichter, W. Analytic Optimal Observability Maneuvers for In-Orbit Bearings-Only Rendezvous. *J. Guid. Control Dyn.* **2014**, *37*, 1658–1664. [CrossRef]

23. Mok, S.-H.; Pi, J.; Bang, H. One-step rendezvous guidance for improving observability in bearings-only navigation. *Adv. Space Res.* **2020**, *66*, 2689–2702. [CrossRef]

24. Hou, B.; Wang, D.; Wang, J.; Ge, D.; Zhou, H.; Zhou, X. Optimal Maneuvering for Autonomous Relative Navigation Using Monocular Camera Sequential Images. *J. Guid. Control Dyn.* **2021**, *44*, 1947–1960. [CrossRef]

25. D'Amico, S.; Ardaens, J.S.; Gaias, G.; Benninghoff, H.; Schlepp, B.; Jorgensen, J.L. Noncooperative Rendezvous Using Angles-Only Optical Navigation: System Design and Flight Results. *J. Guid. Control Dyn.* **2013**, *36*, 1576–1595. [CrossRef]

26. Pesce, V.; Opromolla, R.; Sarno, S.; Lavagna, M.; Grassi, M. Autonomous relative navigation around uncooperative spacecraft based on a single camera. *Aerosp. Sci. Technol.* **2019**, *84*, 1070–1080. [CrossRef]

27. Clohessy, W.H.; Wiltshire, R.S. Terminal Guidance System for Satellite Rendezvous. *J. Aerosp. Sci.* **1960**, *27*, 653–658. [CrossRef]

28. Okasha, M.; Newman, B. Guidance, Navigation and Control for Satellite Proximity Operations using Tschauner-Hempel Equations. *J. Astronaut. Sci.* **2013**, *60*, 109–136. [CrossRef]

29. Yamanaka, K.; Ankersen, F. New State Transition Matrix for Relative Motion on an Arbitrary Elliptical Orbit. *J. Guid. Control Dyn.* **2002**, *25*, 60–66. [CrossRef]

30. Arthur, G. *Applied Optimal Estimation*; The MIT Press: Cambreidge, MA, USA, 1974.